Endogenous pannexin1 channels form functional intercellular cell–cell channels with characteristic voltage-dependent properties

Nicolás Palacios-Prado[a,b,1] (ID), Paola A. Soto[a], Ximena López[a], Eun Ju Choi[c], Valeria Marquez-Miranda[d], Maximiliano Rojas[e], Yorley Duarte[b,e], Jinu Lee[c], Fernando D. González-Nilo[b,e] (ID), and Juan C. Sáez[a,b,1]

The occurrence of intercellular channels formed by pannexin1 has been challenged for more than a decade. Here, we provide an electrophysiological characterization of exogenous human pannexin1 (hPanx1) cell–cell channels expressed in HeLa cells knocked out for connexin45. The observed hPanx1 cell–cell channels show two phenotypes: O-state and S-state. The former displayed low transjunctional voltage (V_j) sensitivity and single-channel conductance of ~175 pS, with a substate of ~35 pS; the latter showed a peculiar dynamic asymmetry in V_j dependence and single-channel conductance identical to the substate conductance of the O-state. S-state hPanx1 cell–cell channels were also identified between TC620 cells, a human oligodendroglioma cell line that endogenously expresses hPanx1. In these cells, dye and electrical coupling increased with temperature and were strongly reduced after hPanx1 expression was knocked down by small interfering RNA or inhibited with Panx1 mimetic inhibitory peptide. Moreover, cell–cell coupling was augmented when hPanx1 levels were increased with a doxycycline-inducible expression system. Application of octanol, a connexin gap junction (GJ) channel inhibitor, was not sufficient to block electrical coupling between HeLa KO Cx45-hPanx1 or TC620 cell pairs. In silico studies suggest that several arginine residues inside the channel pore may be neutralized by hydrophobic interactions, allowing the passage of DAPI, consistent with dye coupling observed between TC620 cells. These findings demonstrate that endogenously expressed hPanx1 forms intercellular cell–cell channels and their unique properties resemble those described in innexin-based GJ channels. Since Panx1 is ubiquitously expressed, finding conditions to recognize Panx1 cell–cell channels in different cell types might require special attention.

electrophysiology | unitary events | dye coupling | permeability | dynamic asymmetry

Gap junctions (GJs) are assemblies of intercellular channels formed by oligomerized transmembrane proteins from adjacent cells. Each GJ channel is formed by two hemichannels (HCs) docked in series, and each HC may be composed by six, seven, or eight monomers depending on the monomer identity. GJs are expressed in nearly all tissues and provide metabolic and electrical coupling with wide-ranging physiological relevance. To date, it is well accepted that only two large families of tetra-spanning membrane proteins oligomerize and form GJs, connexin (Cx) and innexin (Inx) superfamilies. The Cx family is exclusively found in vertebrates (chordates), while the Inx family is present in invertebrates (nonchordates). Similar to Cxs, most Inxs are thought to oligomerize forming hexamers; however, cryo-electron microscopy structures from GJ channels formed by Inx6 show that each innexon is formed by eight monomers (1).

In the year 2000, Inx-like proteins, named pannexins (Panxs), were found in vertebrates, raising the possibility that vertebrate cells might express a different type of GJ channel (2, 3). Three members of the Panx family have been described so far; Panx1, Panx2, and Panx3. Interestingly, brain cells such as neurons, oligodendrocytes, astrocytes, and microglia express at least Panx1. Panx1 has been shown to oligomerize, forming heptamers (4), whereas Panx2 oligomerizes into octamers (5). Panxs are glycoproteins that have been widely shown to form functional plasma membrane channels named pannexons or Panx channels (6, 7). However, the formation of functional Panx cell–cell channels in mammalian cell lines and vertebrate tissue is a question of substantial debate (8–10). Since the discovery of Panxs, a relatively small number of publications have shown intercellular communication mediated by Panx cell–cell channels using electrophysiology or permeability tracer techniques (3, 11–15). Several studies regarding permeability and pharmacology of exogenous Panx cell–cell channels have disparate conclusions, and they also differ from data obtained on Panx channels (16–19). Thus, the lack of reproducible data and negative results obtained in cells that

Significance

Pannexin1 is a glycoprotein that has been shown to form functional plasma membrane channels and mediate many cellular signaling pathways. However, the formation and function of pannexin1-based intercellular cell–cell channels in mammalian cells and vertebrate tissue is a question of substantial debate. This work provides robust electrophysiological evidence to demonstrate that endogenously expressed human pannexin1 forms cell–cell channels and lays the groundwork for studying a potential new type of electrical synapses between many mammalian cell types that endogenously express pannexin1.

Author affiliations: [a]Departamento de Fisiología, Pontificia Universidad Católica de Chile, Santiago 6513677, Chile; [b]Instituto de Neurociencias, Centro Interdisciplinario de Neurociencias de Valparaíso, Universidad de Valparaíso, Valparaíso 2360103, Chile; [c]College of Pharmacy, Yonsei Institute of Pharmaceutical Sciences, Yonsei University, Incheon 21983, Korea; [d]Centro de Nanotecnología Aplicada, Facultad de Ciencias, Universidad Mayor, Santiago 8580745, Chile; and [e]Center for Bioinformatics and Integrative Biology, Facultad de Ciencias de la Vida, Universidad Andrés Bello, Santiago 6513677, Chile

[1]To whom correspondence may be addressed. Email: nicopalacios@uc.cl or juancarlos.saez@uv.cl.

endogenously express Panxs led several research groups to reject the possibility that Panxs form intercellular channels under physiological conditions. This scenario has inclined toward an unfounded skepticism that Panx-based cell–cell channels are a mere "academic peculiarity" rather than a "common cellular feature" (20). These opinions have produced a dogmatic view in the GJ research field that is based mainly on the absence of a strong body of work demonstrating intercellular communication mediated by endogenously expressed Panxs and the fact that Panx proteins can be glycosylated at their extracellular loops (ELs). In support to the latter, analysis of Panx1 overexpressed in transformed human kidney cells (tsA201), NRK, or 293T cells before and after deglycosylation test with PNGase F have revealed that both glycosylated and nonglycosylated forms of Panx1 are present under control conditions (4, 10, 21). These studies contributed to propose that glycosylation of Panxs might obstruct the serial docking of adjacent channels due to "structural hindrance" (8, 10, 22). However, it should be considered that differential glycosylation occurs for several membrane proteins expressed in different cell types (23, 24). In fact, glycosylation is a posttranslational modification that shows great heterogeneity since a particular protein found in different microdomains of a single cell could be nonglycosylated or glycosylated to different degrees (25), indicating that glycosylation state is variable. Accordingly, cell proliferation and culture density have been shown to affect the activity of N-acetylglucosaminyltransferase (26), suggesting that the state balance of glycosylation is a dynamic process depending on environmental and cellular conditions. Hence, the fact that Panx1 can be glycosylated does not necessarily indicate that this modification is constant in all Panx1 proteins expressed at any given time and, furthermore, specific conditions that favor the formation of functional cell–cell channels remain to be identified.

In the present work, we systematically studied properties of macroscopic and single-channel transjunctional currents of human Panx1 (hPanx1) cell–cell channels. First, we used hPanx1 HeLa cell transfectants that do not express other GJ-forming proteins found in vertebrate cells. Then, the same measurements were performed in a human oligodendroglioma cell line (TC620) that endogenously expresses Panx1 where cell–cell channels showed electrophysiological features similar to those found in hPanx1 HeLa cell transfectants. This finding was further supported by the resistance of the cell–cell coupling to octanol (Oct), a well-known blocker of GJ channels formed by Cxs. Following previous recommendations (8), and because of a lack of evidence for hPanx1 to form assemblies of intercellular channels into GJ-like structures, we decided to specifically use the name Panx cell–cell channel to refer to the formation of an intercellular channel made by Panx, and Panx1 HCs only to refer to both hemichannels that are already docked into a cell–cell channel.

Results

HeLa Cells Transfected with hPanx1 Exhibit Two Different States of Electrical Coupling.
To characterize the electrophysiological properties of hPanx1 cell–cell channels we used a genetically modified HeLa cell line in which endogenous Cx45 was knocked out (HeLa KO Cx45) (27). We transfected these cells with a pIRES2-EGFP vector in which wild-type hPanx1 and enhanced green fluorescent protein (EGFP) are expressed separately. The presence of both glycosylated and nonglycosylated forms of hPanx1 in HeLa KO Cx45 cells was detected by immunoblot (*SI Appendix*, Fig. S1).

Double whole-cell patch-clamp experiments were performed using spontaneously generated HeLa KO Cx45–hPanx1 cell pairs within cultures with ≥80% confluence. The transjunctional voltage (V_j) sensitivity of junctional conductance (g_j) was first examined using a stepwise V_j protocol from -100 to $+100$ mV, applied in 20-mV increments of 2.5 s in duration, respectively. A prepulse step of -20 mV was applied before each voltage step to monitor for changes in g_j during the time course of V_j protocol (45 s).

Steady-state junctional currents (I_j) in HeLa KO Cx45–hPanx1 cell pairs showed two distinct phenotypes (activity states), one with averaged total $g_j = 7.4 \pm 1.4$ nS (measured at -20 mV), observed in 55.5% of coupled pairs ($n = 38$) that exhibited low sensitivity to V_j (*SI Appendix*, Fig. S2 A and B), and another type with lower coupling, which corresponded to 44.5% of coupled pairs, with an averaged total $g_j = 0.89 \pm 0.28$ nS (measured at -20 mV) that exhibited higher V_j sensitivity and asymmetry on g_j–V_j dependence according to the sequence order of the V_j protocol (*SI Appendix*, Fig. S2 C and D). These two distinct V_j-dependent phenotypes were also observed while applying continuous V_j ramps from -100 to $+100$ mV (5 s in duration) and then from $+100$ to -100 mV (Fig. 1 A–D).

For the high-V_j-sensitivity phenotype, fitting of the g_j–V_j relationship when V_j protocol starts at -100 mV (*SI Appendix*, Fig. S2D, *Left*) using a two-state Boltzmann equation (28); *SI Appendix*, Fig. S2 legend) produces the following values for hemichannels (1, 2): $A_1 = 0.050$ mV^{-1}; $Vo_1 = 7.6$ mV; $A_2 = 0.6$ mV^{-1}; $Vo_2 = 39.5$ mV. Fitting of the g_j–V_j relationship when V_j protocol started at $+100$ mV (*SI Appendix*, Fig. S2D, *Right*) produced the following values for HCs (1, 2): $A_1 = 0.13$ mV^{-1}; $Vo_1 = 37.17$ mV; $A_2 = 0.05$ mV^{-1}; $Vo_2 = 0.63$ mV. Therefore, the Vo_1 parameter is shifted ~30 mV toward negative V_js just by inverting the sequence of the V_j protocol, while Vo_2 is shifted ~38 mV toward positive V_js. Interestingly, some cell pairs showed single-channel events without reducing g_j with pharmacological agents. At the single-channel level we also found two distinct conductances: one with channels exhibiting open-state conductance of $\gamma_o = 175 \pm 8$ pS with low V_j sensitivity (Fig. 1G) and transitions to a substate conductance of $\gamma_s = 35 \pm 4$ pS (Fig. 1 E and G–I) and another phenotype with higher V_j sensitivity and single-channel conductance identical to $\gamma_s = 35 \pm 4$ pS (Fig. 1 F–I), which correspond to the substate of the first observed phenotype.

These results indicate that hPanx1 cell–cell channels expressed in HeLa cells can reside in either one of two distinct states of activity: the O-state, which shows higher total g_j, low V_j sensitivity, and single-channel conductance with open state ($\gamma_o = 175 \pm 8$ pS) and substate ($\gamma_s = 35 \pm 4$ pS), and the S-state, which shows lower total g_j, higher V_j sensitivity, and single-channel conductance ($\gamma_s = 35 \pm 4$ pS) identical to the substate of the O-state. While hPanx1 cell–cell channels reside in the S-state the mechanism of V_j gating is deterministic, where the transition kinetics and dwelling times of open and closed states are history-dependent. In other words, the S-state has a property called long-range correlation or memory (29). We termed this particular memory behavior of hPanx1 cell–cell channels "dynamic asymmetry," since the capacity of the channel to transfer an electric signal to one side or the other of the junction is modulated by previous events.

GJ-Forming Inx Proteins Contain N-Glycosylation Sites at Their ELs.
N-glycosylation located at the ELs of Panxs has been one of the major reasons to suspect that intercellular docking of Panx1 channels does not occur under physiological conditions
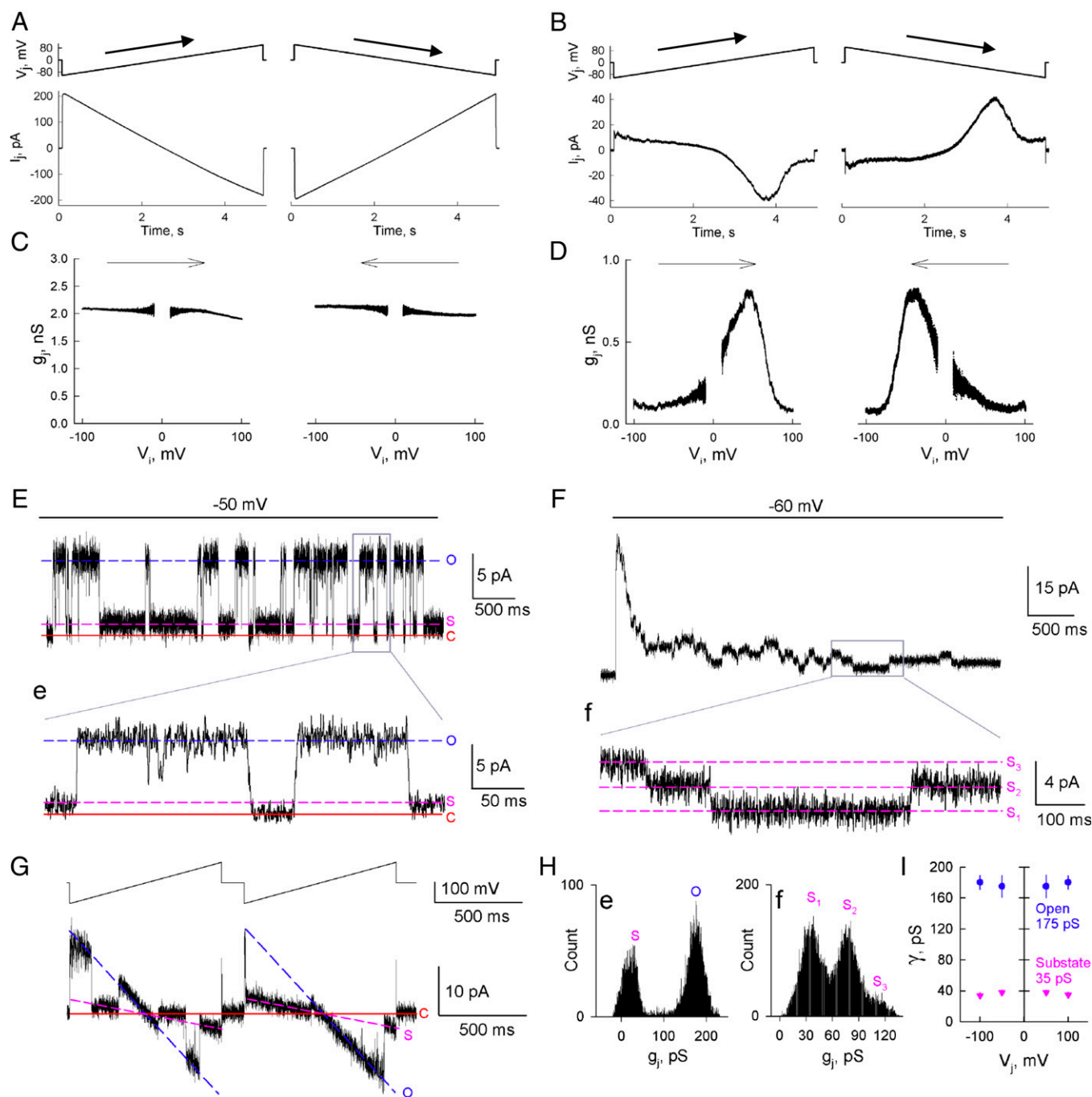
Fig. 1. hPanx1 cell–cell channels can exhibit a main V_j-insensitive open state and/or a V_j-sensitive substate producing dynamic asymmetry. (*A*) Transjunctional current (I_j) traces of an electrically coupled HeLa cell pair expressing wild-type hPanx1 in response to V_j ramps from −100 to +100 mV (*Left*) and from +100 to −100 mV (*Right*) in the same cell pair. This phenotype (*O*-state) shows little V_j sensitivity. (*B*) Another cell pair subjected to the same V_j protocol shown in *A* exhibiting a different phenotype (*S*-state) with enhanced V_j sensitivity and dynamic asymmetry. (*C* and *D*) g_j–V_j relationships calculated from data shown in *A* (*C*) or *B* (*D*). Arrows indicate the time-course direction of V_j ramps. (*E*) I_j record with a single hPanx1 cell–cell channel at $V_j = -50$ mV showing main open (O, blue dashed line), substate (S, magenta dashed line), and closed (C, red line) states. This channel configuration corresponds to the *O*-state shown in *A*. The rectangular inset is time-magnified in **e**. (*F*) I_j record showing multiple single hPanx1 cell–cell channel events between substates at $V_j = -60$ mV. This configuration corresponds to the *S*-state shown in *B*. The rectangular inset is time-magnified in **f**. (*G*) I_j record of a single hPanx1 cell–cell channel in response to two consecutive V_j ramps from −100 to +100 mV showing transitions between main open (O), substate (S), and closed (C) state. (*H*) All-point amplitude histograms (counts) for g_j calculated from I_j traces shown in **e** and **f**. (*I*) Averaged single cell–cell channel conductance (γ) for open state (175 ± 8 pS) and substate (35 ± 4 pS) at different V_js.

(8, 10). Hence, we performed a bioinformatic search of genomic data to analyze the presence of glycosylation sites in the amino acid sequences of seven Inxs from *Caenorhabditis elegans* and three Inxs from *Drosophila melanogaster* that have been shown to form GJ channels under physiological conditions (30–36), and we compared these with hPanx1. We aligned the amino acid residues sequence of EL1 and EL2 and highlighted

all predicted *N*-glycosylation sites within ELs (*SI Appendix*, Fig. S3). No glycosylation sites were predicted for Inx3 with NetN-Glyc server, although Bioiluminate did find a consensus motif at N219. These findings indicate that the presence of *N*-glycosylation sites at ELs of these Inxs-based GJ channels, and possibly Panx1 too, is not a condition that abrogates the formation of intercellular channels.

3 of 11

TC620 Cells Express Panx1 and Show Dye Cell–Cell Coupling.
To find intercellular channels formed by endogenously expressed Panx1 we searched for a human cell line that expresses endogenous Panx1 and exhibits cell-to-cell transfer of permeability tracers using the so-called dye coupling technique. Expression of endogenous glycosylated and nonglycosylated forms of hPanx1 were detected by immunoblot in TC620 cells (*SI Appendix*, Fig. S4 *G and H*). Dye-coupling experiments were performed using monolayers of TC620 cells by injecting different dyes into one cell and recording their transfer to neighboring cells. Dye fluorescence emission was evaluated ~5 min after injection, and the coupling index was calculated. At resting conditions and 30 °C in the bathing solution, we found dye coupling between TC620 cells only with DAPI (4′,6-dia-midino-2-phenylindole), but it was very low with Lucifer yellow (LY), ethidium bromide (Etb), or propidium iodide (Ppd) (*SI Appendix*, Fig. S4 *A–E*).

The coupling index of DAPI transfer was slightly reduced (nonsignificant) when cells were pretreated over 10 min with Oct (*SI Appendix*, Fig. S4F). However, 24-h pretreatment with [10]Panx1 strongly reduced the DAPI coupling index (*SI Appendix*, Fig. S4F), indicating that intercellular DAPI transfer between TC620 cells was mediated by endogenous Panx1 cell–cell channels. Moreover, the DAPI coupling index was not affected after 24-h pretreatments with the Cx-based GJ mimetic peptide inhibitor Gap26 or control scrambled peptide (*SI Appendix*, Fig. S4F). In addition, we found that the DAPI coupling index between TC620 cells is increased fivefold by raising the bath temperature from 20 °C to 30 °C (Fig. 2 *A and B*).
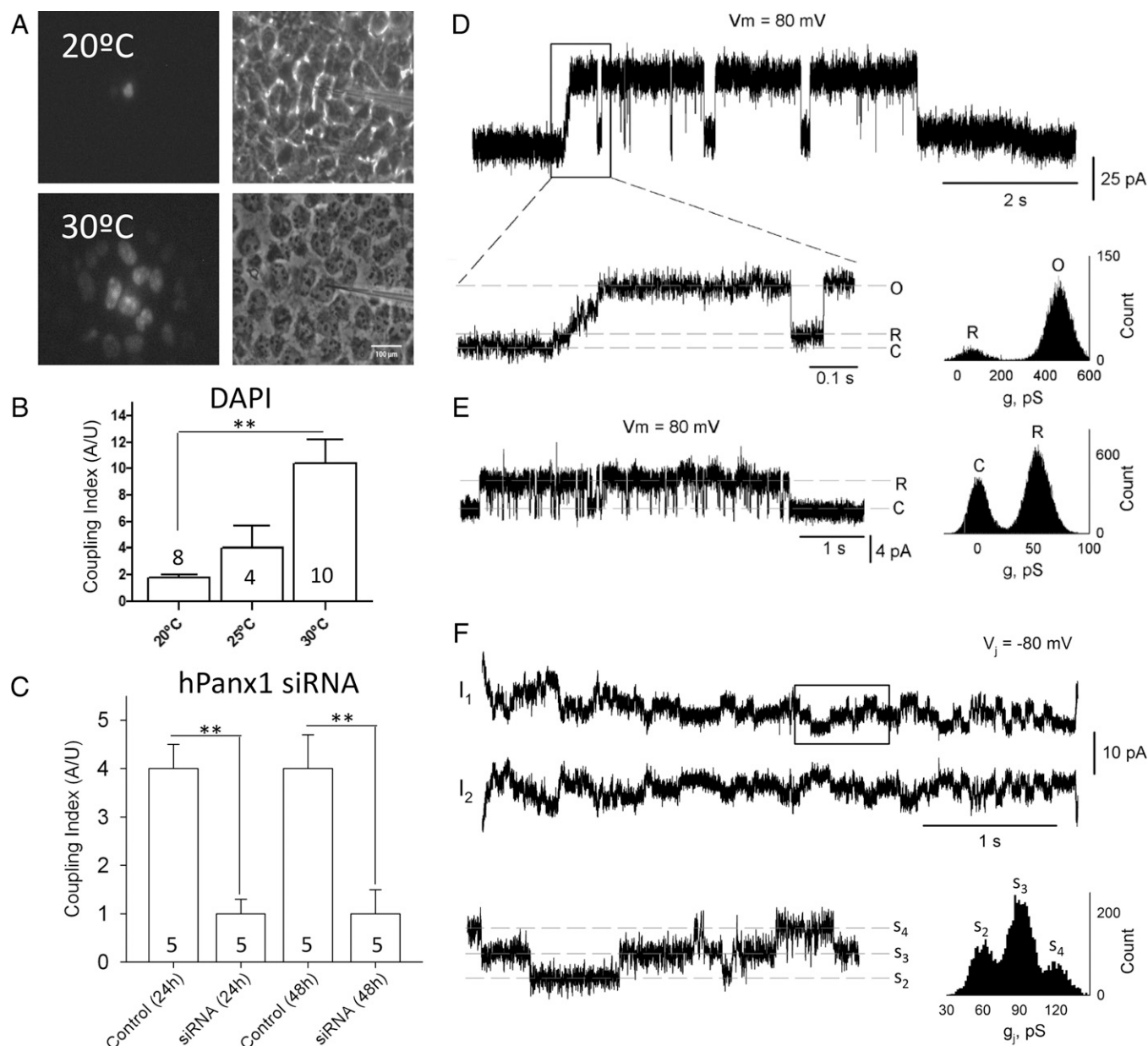
The Extent of Electrical Cell–Cell Coupling in TC620 Cells Depends on Culture Confluence and Temperature. Experiments were performed using spontaneously preformed TC620 cell pairs in cultures grown for 24 to 29 h or more at 20, 50, and 80% confluence. Since cell proliferation and culture density have been shown to affect the activity of *N*-acetylglucosa-minyltransferase (26), we studied whether cell density in TC620 cultures affects the ability to form intercellular channels. We found that electrical coupling at 20 °C appears in few cell pairs after reaching ~50% confluence. However, ~50% of all cell pairs analyzed showed electrical coupling after reaching ≥80% confluence (*SI Appendix*, Fig. S5). TC620 cell pairs showed typically low electrical coupling, fast and noisy trans-junctional current fluctuations, and stepwise cell–cell channel activity of 36 ± 3 pS (Fig. 2F).

After finding that a cell pair is electrically coupled, we performed outside-out excised patch experiments to analyze whether Panx1 channel activity was present. These membrane patches exhibited single-channel events that corresponds to single Panx1 channels (18, 19, 37–39). Normally, at membrane potential of +80 mV, we detected single-channel events with conductance of 65 ± 4 pS (Fig. 2E). However, in a few patches (*n* = 3) we also detected single-channel events with open-state conductance of ~480 pS and residual state (substate) of ~65 pS at +80 mV (Fig. 2D). This residual state corresponds to single Panx1 channels at positive membrane potentials, and the fully open state corresponds to the large-conductance Panx1 channels, mostly found under pathological conditions or using high extracellular potassium gluconate (16, 40, 41). Interestingly, our recordings show a clear time-course difference in the transition between closed state and fully open state with ~100 ms (slow gate) and a very fast transition (unresolved) between fully open and residual states (Fig. 2D).

Typically, in high-confluence cultures, TC620 cells presented a mean value of total junctional conductance (G$_j$), measured at V$_j$ = −20 mV, of 0.4 ± 0.08 nS, varying from 0.1 to 0.6 nS (Fig. 3B and *SI Appendix*, Fig. S6). We also tested whether bath temperature affects electrophysiological properties of cell–cell channels. If coupled TC620 cell pairs were subjected to an increase in bath temperature from 20 °C to 30 °C (5 min), the normalized junctional conductance measured at V$_j$ = −20 mV increased twofold during the time course of the experiment (~10 min) (Fig. 3 *A–C*). Moreover, if the bath temperature was increased during recordings of cell pairs that were not electrically coupled at 20 °C, after 15 min of increasing temperature to 30 °C single cell–cell channels activity appeared during the recording (Fig. 3D), revealing an averaged single cell–cell channel conductance (γ$_s$) of 36 ± 3 pS at 20 °C and 38 ± 4 pS at 30 °C (Fig. 3 *D–F*). We did not find a significant difference of γ$_s$ at the two temperatures studied or at different V$_j$ intensities or polarity (Fig. 3 *E and F*). Nonetheless, we did find an unusual disparity in open probability (P$_o$) when first measured at V$_j$ = −50 mV (P$_o$ = 0.03) and then measured at V$_j$ = +50 mV (P$_o$ = 0.3) (Fig. 3G).

Endogenous Panx1 Expression Is Necessary for Dye and Electrical Cell–Cell Coupling between TC620 Cells. To study whether endogenous expression of Panx1 in TC620 cells is required for dye and electrical coupling, we transfected a small interfering RNA (siRNA) against hPanx1 in TC620 cultures. After 48 h of transfection, the relative amount of Panx1 was reduced compared to control cells transfected with scramble siRNA (*SI Appendix*, Fig. S4I). Coupling was evaluated after 24 and 48 h of siRNA transfection in TC620 cell cultures. DAPI coupling and total junctional conductance were greatly reduced when endogenous expression of Panx1 was hindered by siRNA transfections (Fig. 2C and *SI Appendix*, Fig. S6 *A and B*). In contrast, the percent of electrically coupled pairs and total junctional conductance was increased when wild-type hPanx1 was expressed in TC620 cells using a Tet-On 3G doxycycline (Dox)-inducible gene expression system (*SI Appendix*, Figs. S4G and S6 *A and B*). Dox (500 ng/mL) was added to culture media 24 h before experiments. The HeLa KO Cx45 cell line did not show electrical coupling under control conditions (*SI Appendix*, Fig. S6 *A and B*), but when hPanx1 was overexpressed more than 80% of evaluated cell pairs showed electrical coupling in confluent cultures (*SI Appendix*, Fig. S6 *A and B*), and total junctional conductance measured at V$_j$ = −20 mV reached 5.5 ± 1.5 nS, more than a 12-fold increase compared to confluent parental TC620 cell cultures (*SI Appendix*, Fig. S6B).

Electrical Cell–Cell Coupling in TC620 cells Is Resistant to Oct and Panx1 Hemichannel Blockers. We study changes in electrical coupling in TC620 cells treated with 1 mM Oct (a general Cx-based GJ blocker), 100 µM probenecid (PBN, a Panx1 channel blocker), or 50 µM carbenoxolone (CBX, a blocker of Cx-based GJ channels and HCs as well as Panx1 channels) (42). Application of Oct (~5 min) did not significantly affect the electrical coupling either in parental TC620 or HeLa KO Cx45– hPanx1 cell pairs (*SI Appendix*, Fig. S6 *D and E*). These results are consistent with previous reports about insensitivity of Panx1-EGFP intercellular channels to heptanol treatments in HeLa cells (14). Moreover, application of either CBX or PBN were also insufficient to block electrical coupling, although 2-min exposure to CBX induced a ~30% or ~15% inhibition in TC620 or HeLa KO Cx45– hPanx1 cell pairs,

Fig. 2. TC620 cells show dye and electrical cell–cell coupling. (*A*) Fluorescence (*Left*) and bright-field (*Right*) images of TC620 cell cultures after 5 min of DAPI injection at 20 °C (*Upper*) and 30 °C (*Lower*). (*B*) DAPI coupling index quantification in TC620 cells at different bath temperatures. (*C*) Effect of siRNA transfection against hPanx1 on coupling index after 24 or 48 h of transfection. Numbers at the bottom of each bar represent the number of independent cell pairs; **$P < 0.005$. (*D*) Unusual current record from outside-out excised patch with single hPanx1 hemichannel activity showing a slow transition between a closed state (C) and a fully open state (O) of 480 pS, and fast transitions between O and a residual state (R) of 65 pS, at 80 mV. (*E*) Current record from outside-out excised patches showing transitions between C and R states of 65 pS at 80 mV. (*F*) Records of endogenous electrical coupling between TC620 cell pair showing current traces for cell 1 (I_1) and cell 2 (I_2) while holding voltage at −80 mV in cell 1 and at 0 mV in cell 2 ($V_j = -80mV$). Bottom trace shows magnification of the rectangular inset depicting transition events of hPanx1 cell–cell channels. Dashed lines marked substate levels from 2 to 4. Count histogram of junctional conductance (g_j) calculated from inset showing peaks for channels substate 2 to 4 with averaged $\gamma = 35 \pm 0.3$ pS.

respectively (*SI Appendix*, Fig. S6 *C–E*), and 2 min application of PBN during recordings induced a ~18% or ~14% inhibition in TC620 or HeLa KO CX45–hPanx1 cell pairs, respectively (*SI Appendix*, Fig. S6 *D–E*).

Voltage Dependence of Endogenous and Exogenous hPanx1 Cell–Cell Channels in TC620 Cells Shows "Dynamic Asymmetry" in the g_j–V_j Relationship. Experiments were performed in TC620 cell pairs present in ≥80% confluent cultures, and the V_j sensitivity of g_j was examined using the same stepwise V_j protocol described in *SI Appendix*, Fig. S2. Steady-state junctional currents (I_j) in TC620 cell pairs showed asymmetry in V_j dependence (Fig. 4 *A* and *B*). Fitting of the g_j–V_j

relationship when V_j protocol started at −100 mV (Fig. 4*B*, *Left*) using a two-state Boltzmann equation (28) (*SI Appendix*, Fig. S2 legend) produced the following values for HCs (1, 2): $A_1 = 0.052$ mV^{-1}; $Vo_1 = 7.93$ mV; $A_2 = 0.075$ mV^{-1}; $Vo_2 = 43.3$ mV. Fitting of g_j–V_j relationship when V_j protocol started at +100 mV (Fig. 4*B*, *Center*) yielded the following values for HCs (1, 2): $A_1 = 0.078$ mV^{-1}; $Vo_1 = 39.3$ mV; $A_2 = 0.045$ mV^{-1}; $Vo_2 = 9.7$ mV. Therefore, hPanx1 cell–cell channels in TC620 cells also show dynamic asymmetry and apparently operate in the *S*-state observed in exogenous hPanx1 cell–cell channels between HeLa cells (*SI Appendix*, Fig. S2 *C*). However, fitting of the g_j–V_j relationship when the V_j protocol started at 0 mV and then alternating consecutive 20-mV increments were
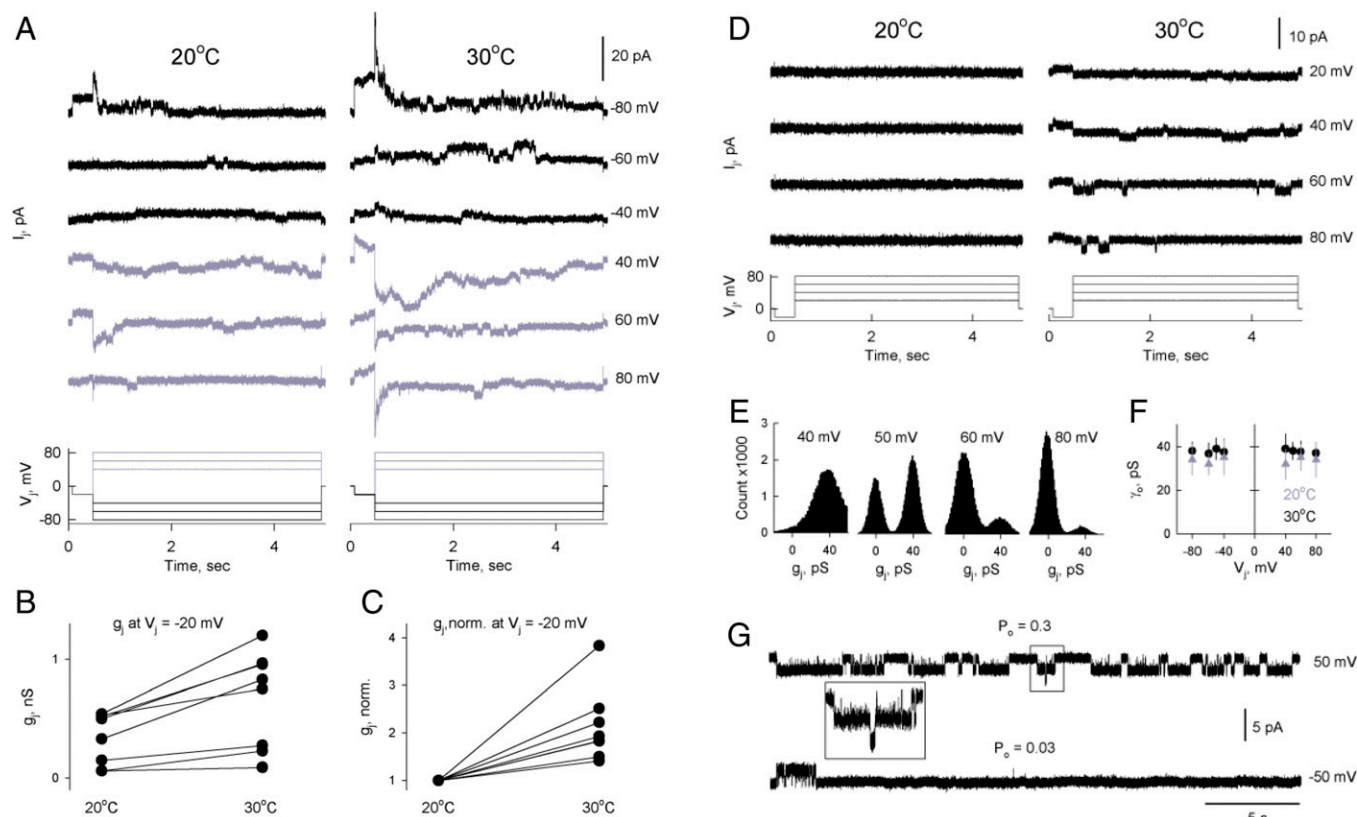
Fig. 3. Effect of temperature on total junctional conductance and functional hPanx1 cell–cell channels. (*A*) Representative transjunctional current (I$_j$) traces of an electrically coupled TC620 cell pair in response to a V$_j$ step protocol from −80 mV to +80 mV and of 4.5 s in duration (*Bottom*). Bath temperature was kept at 20 °C (*Left*) and then increased up to 30 °C (*Right*). (*B*) Dots show calculated g$_j$ at V$_j$ = −20 mV with bath temperature of 20 °C or 30 °C. Lines connect each independent cell pair from measurements from 20 °C to 30 °C. (*C*) Normalized g$_j$ at 20 °C showing an average g$_j$ increase of twofold after increasing bath temperature up to 30 °C. (*D*) Representative I$_j$ traces measured at different V$_j$ of a TC620 cell pair that shows no electrical coupling at 20 °C (*Left*), but single cell–cell channel events appear after increasing temperature up to 30 °C (*Right*). (*E*) Calculated count histograms of g$_j$ for traces of 4 s in duration and at different V$_j$s. (*F*) Mean single cell–cell channel conductance (γ$_o$) measured at different V$_j$s and bath temperatures corresponds to the *S*-state. (*G*) Representative I$_j$ traces showing differential open probability (P$_o$) for single cell–cell channel events (two channels) first measured at −50 mV and then at +50 mV.

applied in either polarity until reaching −100 and +100 mV (Fig. 4*B*, *Right*) using a two-state Boltzmann equation produced the following values for HCs (1, 2): $A_1 = 0.051$ mV^{-1}; $Vo_1 = 17.7$ mV; $A_2 = 0.036$ mV^{-1}; $Vo_2 = 15.6$ mV. Therefore, just by alternating the polarity of incremental V$_j$ steps, which alternates ionic current flow through the cell–cell channel pore, produces a rather symmetric g$_j$–V$_j$ relationship.

The observed "dynamic asymmetry" in the g$_j$–V$_j$ relationship was even more accentuated when short-duration V$_j$ ramp protocols were applied (*SI Appendix*, Fig. S7 *A and B*), meaning that the memory property is a short-term memory. Since this asymmetry produced by one specific sequence of V$_j$ steps can be reversed by the opposite sequence, we wanted to verify whether the hPanx1 cell–cell channels have hysteretic behavior. Many voltage-gated channels that display memory properties also display hysteresis in their activity (43), including some Cx-based GJ channels (44). To test for hysteresis in electrically coupled pairs of TC620 cells we applied a long V$_j$ ramp (30 s in duration) from 0 to ±100 mV and back to 0 mV (*SI Appendix*, Fig. S7*C*). The g$_j$–V$_j$ relationship obtained with this protocol revealed that hPanx1-based cell–cell channels exhibit strong hysteresis while residing at the *S*-state (*SI Appendix*, Fig. S7*D*).

Protonation State of Arginine Residues within the Selectivity Filter May Act as a Regulator of the Translocation of DAPI across the Panx1 Cell–Cell Channel. To study how a positively charged molecule, such as DAPI, can permeate an hPanx1 cell–cell channel we built a molecular system consisting of two

Panx1 channels forming a cell–cell channel-like structure. Then, we placed the DAPI molecule in the uppermost section of the system, representing the intracellular region of the upper Panx1 HC (Panx1′). The DAPI translocation through Panx1′ and the bottom Panx1 HC (Panx1″) was simulated using the steered molecular dynamics (SMD) method. We studied all possible salt bridges, π–π, π–cation, and π–stacking interactions between DAPI molecule and amino acid residues during its passage through the cell–cell channel pore (*SI Appendix*, Fig. S8).

As we previously reported, the intracellular region of Panx1 HC is a zone of negative electrostatic potential (45). Thus, it is expected that DAPI, which presents a net charge +2 at physiological pH, can be easily attracted by the amino acid residues found in this entry zone. However, the presence of a ring of seven positively charged R75 found at the selectivity filter should slow or prevent the translocation of DAPI from Panx1′ to Panx1″. Therefore, we studied in detail the neighborhood of the selectivity filter and search for possible residue interactions. The W74 residue contributes to a hydrophobic environment, which could greatly reduce the pK$_a$ (negative logarithm of association constant) for R75, as it has been demonstrated experimentally by the groups of Grosman (46) and Niemeyer (47). The experimental work of Grosman and Sepúlveda showed that a pK$_a$ of arginine can be as low as 4 in a hydrophobic environment. Considering this, we built a profile for the pK$_a$ of an arginine at different dielectric constants (Fig. 4*D*). Our calculations show that arginine residue shifts its pK$_a$ according to its environment, obtaining the same conclusion proposed by
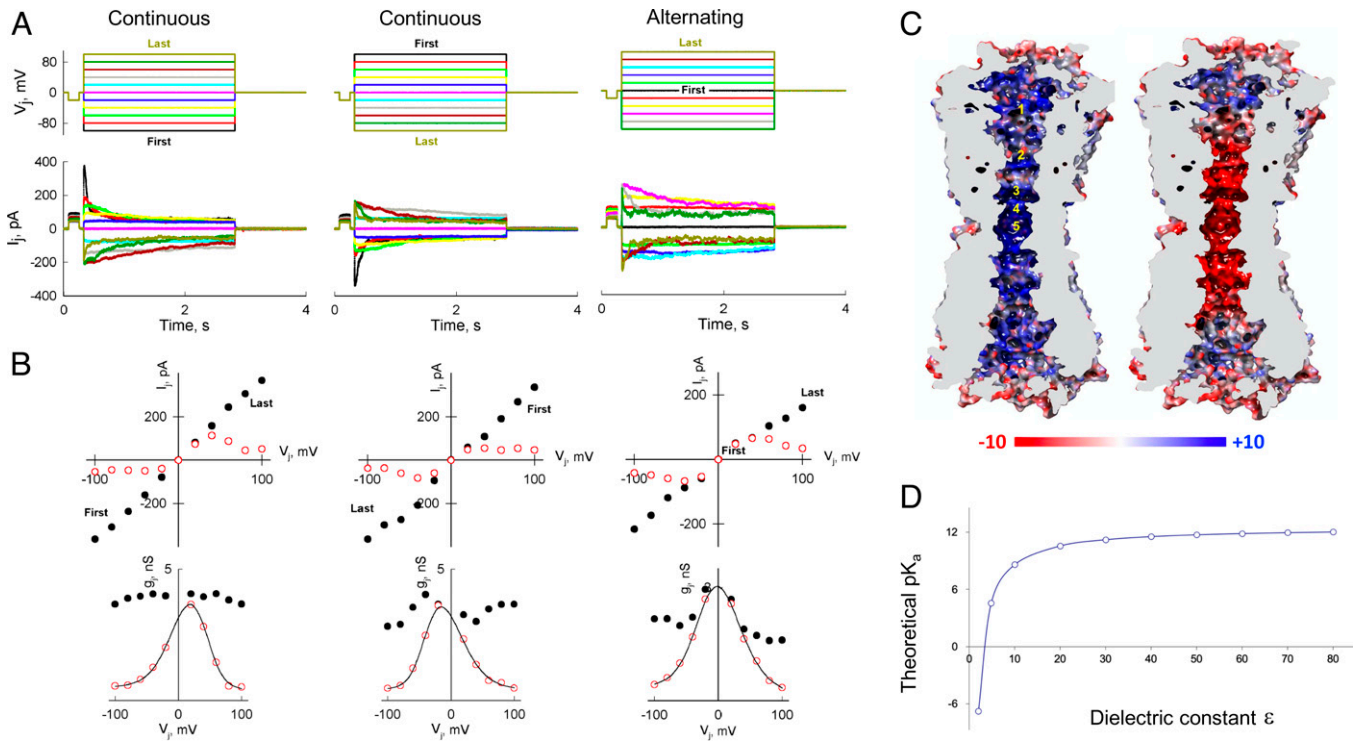
Fig. 4. Dynamic asymmetry observed in pairs of TC620 cells and in silico analysis of electrostatic potential in hPanx1 cell–cell channels. (*A*) Transjunctional current (I_j) traces of an electrically coupled TC620 cell pair in response to "continuous" protocol consisting of consecutive 20 mV V_j steps from −100 to +100 mV (*Left*) or from +100 to −100 mV (*Center*) in the same cell pair (duration of the entire protocol was ~45 s). Another TC620 cell pair (*Right*) subjected to "alternating" protocol consisting of consecutive 20-mV V_j steps with alternating V_j polarity from 0 to −100 and +100 mV. (*B*) Instantaneous (black) and steady-state (red) I_j–V_j (*Top*) and g_j–V_j (*Bottom*) relationships from experiments shown in *A*. Solid lines represent a fit of the data to a two-state Boltzmann equation (*SI Appendix*, Fig. S2 legend). The continuous V_j protocols produce asymmetrical g_j–V_j relationship, while the alternating V_j protocol produces a symmetrical g_j–V_j relationship. (*C*) Cross-sections of cell–cell channels formed by hPanx1 generated by Maestro software. Analysis of electrostatic surface potential in hPanx1 cell–cell channels with protonated (*Left*) or neutral (*Right*) ARG75 residues. The color bar at the bottom represents electrostatic surface potentials ranging from −10 (red) to +10 (blue) kTe^{-1}. (*D*) Profile of dielectric constant versus pK_a of an arginine. Computation of theoretical pK_a was done using second-order Møller–Plesset, and with the density functional theory using the B3LYP method, with the following equation: $pK_a = a \cdot (exp(b/\varepsilon − c)) − d)/\varepsilon$, where a = 12.48, b = −0.01, c = 6.20, and d = 38.61. The solvent was represented using the reaction-field IPCM to obtain solvation free energies. All calculations were performed using Gaussian 09 software.

Grosman and Sepúlveda. In the case of hPanx1, the selectivity filter, placed in a hydrophobic environment with a dielectric close to 10, has the conditions such as the pK_a of arginine residues can be lower than 8, and therefore arginine residues may be in a neutral state. To evaluate the impact of arginine residues deprotonation, we have calculated the electrostatic potential of the inner cavity of hPanx1 cell–cell channel for a state where all the R75 residues are positively charged (Fig. 4*C*, *Left*), as considered in the molecular simulations, and another state, in which all the R75 residues are in a neutral state (Fig. 4*C*, *Right*), as a theoretical representation when two or more arginines are in neutral state. As observed in Fig. 4*C*, the electrostatic potential of the pore changes significantly, going from a positive to a negative environment on the surface of the pore. In summary, the neutralization of arginines of the selectivity filter will promote the DAPI translocation through the hPanx1 channel.

Discussion

Here, we present a systematic electrophysiological characterization of Panx1 cell–cell channels in HeLa cells transfected with hPanx1 and a cell line (TC620) that presents endogenous expression of hPanx1. Previous studies (3, 14) have shown similar, but not identical, pharmacological and electrophysiological properties for exogenous Panx1 cell–cell channels, which are 1) low sensitivity to *n*-alcohols (heptanol and Oct), 2) low V_j sensitivity, 3) a symmetric g_j–V_j relationship, and 4) permeability to

DAPI. However, hPanx1 cell–cell channels expressed in HeLa cells (KO for Cx45) can be found in two different activity states or phenotypes, the *O*-state or *S*-state. Previous studies using exogenous expression systems have described the macroscopic V_j-dependent properties of Panx1 cell–cell channels (3, 14) dwelling in a functional state that we described now as the *O*-state. Here, we add information by providing single-channel records for the *O*-state (Fig. 1 *E* and *F*), in which two conductance states were detected: a low V_j-sensitive main open state ($\gamma_o = 175 \pm 8$ pS) and a substate ($\gamma_s = 35 \pm 4$ pS) (Fig. 1 *C* and *D*). In addition, we characterized a second functional state of hPanx1 cell–cell channels, described as the *S*-state, which has the following properties: 1) resistance to Oct, 2) V_j sensitivity, 3) dynamic asymmetry in the g_j–V_j relationship, 4) unitary conductance identical to the substate of the *O*-state ($\gamma_s = 35 \pm 4$ pS), and 5) permeability to DAPI. Unusual experimental conditions, such as high cell confluence and bath temperature of 30 °C, favored identification of endogenous hPanx1 cell–cell channels between TC620 cells, which show pharmacological and electrophysiological properties identical to the *S*-state cell–cell channels characterized in HeLa cells. All together, these findings indicate that endogenous hPanx1 form functional intercellular channels and have distinctive V_j-dependent properties.

Currently, the available data on unitary conductance of Panx1 channels is rather controversial. Early recordings of Panx1 channels expressed in *Xenopus* oocytes have shown non-rectifying large unitary currents with conductance of ~500 pS and multiple substates (3). A number of other studies have

found similar conductance for Panx1 channels (16, 17, 40). In contrast, data obtained in more recent studies showed that Panx1 channels expressed in mammalian cell lines show rectifying smaller unitary currents with peak conductance of ~90 pS at positive potentials and minimum conductance of ~12 pS at negative potentials (18, 19, 37, 39, 45, 48). These two different activity states of Panx1 channels might be the reason why we identified two different phenotypes in hPanx1 cell–cell channels, here called O-state and S-state. We chose this classification to differentiate from "activated" and "nonactivated" states of Panx1 channels that have been used to distinguish between channels that become permeable or not to adenosine 5′-triphosphate (ATP), respectively (45).

Under experimental conditions with HeLa cells KO for Cx45, we found that permeability to LY is very low in hPanx1 cell–cell channels, as opposed to previous studies (14) that were done in HeLa cells expressing endogenous Cx45 GJs, which are permeable to LY (49). The hPanx1 cell–cell channel properties shown in this study (temperature sensitivity, Oct resistance, and permeability properties) resemble those found in the electric synapses between neurons from *Aplysia*, a noncordate that expresses Inx-based GJs (50, 51). It is important to make a distinction between Cx45 GJs and the S-state of hPanx1 cell–cell channels, since both have similar unitary conductance [~32 pS for Cx45 GJs (52)], but Oct sensitivity is absolutely different [concentration that inhibits response by 50% = 0.025 mM in Cx45 GJs (53)]. Moreover, asymmetric g_j–V_j relationship shown by the S-state of hPanx1 cell–cell channels, resembles asymmetries in GJs formed by Inxs from *D. melanogaster* (54), *Tenebrio molitor* (55), and *Aedes albopictus* (56). To our knowledge there is no report showing a Cx-based GJ channel resistant to 1 mM Oct, indicating that the recorded intercellular channels are composed of a different protein type, likely to be Panx1 because [10]Panx1 and siRNA treatments were effective to reduce cell–cell coupling (Fig. 2 and *SI Appendix*, Figs. S4 and S6).

The glycosylation of EL in Panx1 has been one of the key justifications to support that docking of adjacent Panx1 channels does not occur under physiological conditions. To show that this is not a valid reasoning, we revealed that many well-known GJ-forming Inxs proteins also contain glycosylation sites at their ELs and their predicted glycosylation potentials are similar to hPanx1 (*SI Appendix*, Fig. S3). In addition, another glycosylation site at the EL of Inx3 from the slug *Limax valentianus* has been recently reported (57). Even though N-glycosylation modifications in insects are simpler than in vertebrates (58), these findings support that the presence of glycosylation sites in hPanx1 does not abrogate the formation of intercellular channels.

Since deglycosylation treatments in oocytes expressing Panx1 have been shown to increase electrical coupling (15), it is possible that Panx1 channels at the plasma membrane of cell interfaces may have a differential glycosylation pattern affected by different environmental factors, such as cell culture density (*SI Appendix*, Fig. S5), temperature (Fig. 3), and/or dynamic extracellular glycan remodeling (59). We speculate that the temperature-dependent increase in g_j observed in endogenous hPanx1 cell–cell channels is due to an increased probability for docking of adjacent channels present at the plasma membrane, similarly to the reported temperature-dependent increase in Ic currents from endogenous Cx38 in *Xenopus* oocytes (60). Indirect immunofluorescence analysis shows that localization of Panx1 at the cell membrane is homogeneous, and not as discrete puncta or plaques (12). Ultrastructural studies also have failed to demonstrate Panx1 large plaque-like structures (61), suggesting that Panx1 cell–cell channels might not form the classical crystalline structure formed by Cxs. However, recent cryo-electron microscopy analysis showed fully assembled intercellular channels formed by Panx1 mutants that lacked glycosylation sites (4).

According to our in silico studies, the permeability of Panx1 cell–cell channels to DAPI could require a particular electrostatic potential profile in the pore promoted by neutralization of pore-lining arginine residues by hydrophobic interactions. Interestingly, recent studies have shown that membrane phospholipids can interact with Panx1 channel pore residues (62), providing experimental evidence for a highly hydrophobic and dynamic environment inside the pore. Additional studies will be needed to differentiate in detail the permeabilities of O- and S-states of hPanx1 cell–cell channels and compare those with permeabilities of different conductance and activity states of Panx1 channels.

The confirmation that endogenous hPanx1 forms functional intercellular channels in vertebrate cells is of paramount importance for the GJ and electrical synapses research fields. Many behavioral changes have been reported when Panx1 is knocked out, such as hearing loss (63, 64), increased susceptibility for atrial fibrillation (65), impaired light response in the retina (66), disrupted sleep–wakefulness cycle (67), decreased epileptic activity (68), and modulated hippocampal synaptic plasticity (69). Our data could give some explanation for long-held unknowns in the electrical synapses research, given that many electrical synapses between interneurons in Cx36 KO mice show unusual biophysical properties, such as an asymmetric G_j–V_j relationship (70, 71), and the expression of Panx genes overlaps with brain regions where electrical synapses exhibits a high degree of coupling, including different types of interneurons (72). In addition, asymmetric activity of electrical synapses is a fundamental and dynamic property that has been shown to expand the set of outputs of electrically coupled neuronal networks (73). Finally, since most nervous system cell types of vertebrates express at least one type of Cx and Panx protein, it would be relevant to study the possible coexistence of both types of intercellular channels and to differentiate the possible functional roles of the O-state and S-state of hPanx1 cell–cell channels. Most likely these final issues will be areas of intense research in the near future.

Materials and Methods

Reagents. CBX, Oct, PBN, +β-glycyrrhetinic acid, and doxycycline (ready-made) were acquired from Sigma-Aldrich. DAPI, LY, Etd, and Ppd were purchased from Invitrogen. Dulbecco's modified Eagle's medium (DMEM) and RPMI 1640 culture medium were purchased from Gibco, and TurboFect reagent was from Thermo Scientific, the three brands belonging to Thermo Fisher Scientific. The RNA silencing tool, Panx1 siRNA and its corresponding control solution, was purchased from Qiagen (FlexiTube GeneSolution). The inhibitory Panx1 mimetic peptide ([10]Panx1), Gap26, and scrambled peptide (S-peptide) were obtained from NeoMPS (San Diego). A previously described polyclonal anti-Panx1 antibody was used (74). Anti-Panx1 (91137; Cell Signaling Technology) and anti-actin (sc-376421; Santa Cruz Biotechnology) antibodies were also used.

Dye Coupling. Dye-coupling experiments were performed by microinjection of fluorescent dyes as previously described (75). Briefly, cells grown on glass coverslips were transferred to an experimental chamber mounted on the stage of a Nikon fluorescence microscope equipped with a digital camera and imaging system. Appropriate excitation and emission filters (Chroma Technology) were used to acquired images of fluorescence emission for DAPI, LY, Etd, or Ppd microinjected in one cell of a cluster and coupling index that corresponds to the average number of cells to which the dye spread from the microinjected cell in successful trials was evaluated as previously described (75).

Electrophysiology. Electrophysiological recordings were performed in bath solution containing (in millimolar) NaCl, 140; KCl, 5; CaCl$_2$, 1.8; MgCl$_2$, 1; BaCl$_2$, 2; and Hepes, 5 (pH 7.4). Patch pipettes were filled with an intracellular solution containing (in millimolar) CsCl, 130; NaAsp, 10; MgCl$_2$, 1; CaCl$_2$, 0.2; EGTA, 2; and Hepes, 5 (pH = 7.2). We used pipettes with resistances between 4 and 7 MΩ, made with a P-97 puller (Sutter Instruments). Cells were grown onto glass coverslips and transferred to an experimental chamber (Warner Instruments) mounted on the stage of an inverted microscope (IX70; Olympus) equipped with a light-emitting diode–based low-noise fluorescence imaging system (pE Excitation System; CoolLed), camera (Rolera Bolt, Q-Imaging Scientific CMOS) and MetaFluor imaging software (version 7.8.4.0; Molecular Devices). Cells were constantly perfused with extracellular solution using a gravitation perfusion system. Temperature of bath solution was kept constant at 20°, 25°, or 30 °C using a temperature controller (CU-301 and HIS-101; Live Cell Instruments). Junctional conductance (g$_j$) was measured in randomly selected cell pairs using the dual whole-cell patch clamp system, as previously described (76). The voltage in cell 1 (ΔV_1) was stepped while the voltage in cell 2 was kept constant, and junctional current (I$_j$) was measured as the negative of the change in current in cell 2, I$_j$ = $-\Delta I_2$. Junctional conductance (g$_j$) was given as $-I_j/\Delta V_1$. Signals were acquired and amplified using a 16-bit data acquisition system (Digidata 1322A; Axon Instruments) and amplifier (Multiclamp 700B; Molecular Devices). All signals were recorded and analyzed using pClamp software from Axon Instruments.

Transfections. For transient transfection of hPanx1 we used HeLa cells knocked out for Cx45 (HeLa KO Cx45), where the expression of endogenous Cx45 was ablated with CRISPR/Cas9 (27). HeLa KO Cx45 cells were transfected with a pIRES2-EGFP-hPanx1 vector (plasmid was generated by insertion of the hPanx1 CDS into Xho1/EcoR1 site of pIRES2-EGFP) that induces separate expression of wild-type hPanx1 and EGFP, as follows: 400 μL of DMEM, 4 to 8 μg of DNA was resuspended and 6 μL of TurboFect reagent (Thermo Fisher) was added. The mixture was incubated for 20 min at room temperature and subsequently added by dripping onto cell cultures that had been seeded in glass coverslips of 25 mm diameter at >50% confluence.

Generation of Lentiviral Plasmids. A lentiviral plasmid, pLVX-TRE3G-hPanx1 that expresses hPanx1 in a Dox-inducible manner was generated by introduction of hPanx1 CDS into pLVX-TRE3G (Clontech).

Generation of Stable Cell Lines. Lentivirus was used to stably express transgenes. To produce lentivirus, HEK293T cells were transfected with a 4:3:1 mixture of a lentiviral plasmid, psPAX2 (Addgene 12260) and pMD2.G (Addgene 12259). The media conditioned with the transfected HEK293T cells for 48 h were harvested, cleared by filtration through a 0.45-μm pore filter, and stored at 4 °C before use. The lentiviruses used in this study includes pLVX-EF1α-Tet3G and pLVX-TRE3G-hPanx1. TC620 cells were transduced with pLVX-EF1α-Tet3G virus and selected with 1 mg/mL of G418 (AG Scientific) for a week. Then, the surviving cells were treated with pLVX-TRE3G-hPanx1 virus and selected with 1 μg/mL with puromycin (Sigma) for another week, leading to TC620-ind-hPanx1 cells.

Western Blot. hPanx1 was detected as described previously (74). In brief, parental or transfected cells were harvested using a rubber policeman on icecold saline solution. Then, cells were pelleted and lysed with phosphate-buffered saline containing 1% Triton X-100 and 1x complete protease inhibitor mixture (Roche) followed by centrifugation at 4 °C with 13,000 rpm for 15 min. The protein concentration of the supernatants was determined with a BCA assay kit (Sigma). The lysates were separated in 8% sodium dodecyl sulfate polyacrylamide gels and transferred to nitrocellulose membrane before detection with anti-Panx1 or anti-actin antibody.

Identification of *N*-Glycosylation Sites within Inxs Sequences. First, we generated multiple sequence alignments for seven Inxs from *C. elegans* and three Inxs from *D. melanogaster* that are well-known GJ forming proteins (*SI Appendix*, Fig. S3). The amino acid residues sequence of EL1 and EL2 of Inxs were aligned using Multiple Sequence Viewer of Schrodinger (BioLuminate; Schrödinger, LLC). To identify glycosylation sites we searched in each sequence for the consensus motif for *N*-glycosylation (Asn-X-Ser/Thr) using the predictor NetNGlyc 1.0 Server (https://services.healthtech.dtu.dk/service.php?NetNGlyc-1.0),

and additionally we used the Schrödinger biologics modeling platform BioLuminate to confirm glycosylation sites.

Molecular Modeling and Molecular Dynamics Simulations. The full-length hPanx1 hemichannel recently released was considered for this study (Protein Data Bank [PDB] ID: 7DWB) (77), which was assembled into a cell–cell channel-like structure obtained by docking two HCs (*SI Appendix*, Fig. S9), using as a model the full-channel PDB ID 6WBN (4). As described before (4), the assembly of two HCs is mediated through the EL2 linker, in which D256, S257, and T258 in the paired subunits form hydrophilic and hydrophobic interactions. A C-terminal region, starting from the D379 residue, was removed from both HCs. As the intercellular channel communicates two cells, the full structure was inserted into two 187- x 187-Å^2 membrane patches of 1-palmitoyl-2-oleoyl-*sn*-glycero-3-phosphocholine (POPC), representing the membranes of each cell. Then, a water box (TIP3P model) was added and neutralized with a concentration of 0.15 mol/L KCl. Dimensions of the final system were 197 × 200 × 292 Å^3 and a total of 890,063 atoms. To model the protein, the Amber19sb force field was used (78); the LIPID 17 force field for POPC molecules (79), the TIP3P model for water (80), and ion parameters reported by Joung and Cheatham were used (81). DAPI molecules were parameterized using the GAFF force field considering a formal charge of +2 (82) and the ANTECHAMBER (83) module of AMBER20 package, as previously described (45). To build the systems, VMD software was used (84). AMBER 20 software (85) was used to perform an energy minimization and subsequent equilibration protocol by 50 ns under NPT ensemble at 310 K. Van der Waals interactions were cut off at 10 Å, considering the dispersion correction for energy and pressure. Electrostatic interactions were computed using particle mesh Ewald under periodic boundary conditions (86), with a cutoff of 10 Å. To keep the temperature constant at 310 K, a velocity rescale (v-rescale) thermostat (87) was employed. A semi-isotropic Berendsen barostat (88) was used to maintain the pressure at 1 bar.

The SMD method (89) was used to simulate the trajectory of a DAPI molecule crossing the intercellular channel in a reasonable calculation time (Movie S1). SMD calculation considers the application of an external force on a dummy atom through a reaction coordinate to study the translocation of DAPI from the intracellular side of the first cell to the intracellular side of the second cell. The reaction coordinate ξ was defined here as the center of the mass distance between the DAPI molecule and the seven CA atoms of the W74 residues located in the selectivity filter, using the same reaction coordinate as in the first pathway.

Electrostatic potential maps were computed using Maestro software of the Schrodinger suite (90). Theoretical pK$_a$ of *N*-ethyl-guanidine from arginine residues was obtained for different dielectric constants using quantum-mechanical calculations (91). A continuum solvation model was considered, considering water to represent arginine residues exposed to an aqueous solvent and chloroform to represent the conditions of a protein core or membrane.

The dissociation constant K$_a$ of an acid HA into the conjugate base A$^-$ and a proton H$^+$ is related to the Gibbs free energy change (ΔG) of this dissociation reaction by

$$\Delta G = -RT \ln K_a = G(H^+) + G(A^-) - G(HA),$$

where R is the molar gas constant and T is the temperature, which in this case was 298 K. Then, the absolute pK$_a$ for the dissociation reaction is described as

$$pK_a = \frac{1}{2.303\,RT}\Delta G.$$

Briefly, the thermodynamics cycle shown in *SI Appendix*, Fig. S10 has to be solved to obtain relative pK$_a$. The cycle establishes a relationship between acid dissociation in the condensed phase (ΔG_{cp}) to the dissociation in the gas phase (ΔG_{gas}) and to the solvation free energies (ΔG_{solv}) of all the chemical species involved.

All calculations were performed at three levels of theory under the 6-31G(d,p) basis set: 1) Hartree–Fock, 2) second-order Møller–Plesset (92), and 3) second-order Møller–Plesset with density functional theory using the B3LYP method (93). A reaction-field IPCM (isodensity polarized continuum model) was used to obtain solvation free energies (94). All calculations were performed using Gaussian 09 software (95).

Statistical Analysis. Bar graphs are shown as the mean value $\pm$ SE. Significant differences between groups were determined using two-way ANOVA with a post hoc test to perform multiple comparisons. The differences were considered

significant at $P < 0.05$ (*$P < 0.05$, **$P < 0.005$, ***$P < 0.001$). The number of independent experiments is shown at the bottom of each bar.

Data Availability. All study data are included in the article and/or supporting information.

1. A. Oshima, K. Tani, Y. Fujiyoshi, Atomic structure of the innexin-6 gap junction channel determined by cryo-EM. *Nat. Commun.* **7**, 13681 (2016).
2. Y. Panchin *et al.*, A ubiquitous family of putative gap junction molecules. *Curr. Biol.* **10**, R473–R474 (2000).
3. R. Bruzzone, S. G. Hormuzdi, M. T. Barbe, A. Herb, H. Monyer, Pannexins, a family of gap junction proteins expressed in brain. *Proc. Natl. Acad. Sci. U.S.A.* **100**, 13644–13649 (2003).
4. Z. Ruan, I. J. Orozco, J. Du, W. Lü, Structures of human pannexin 1 reveal ion pathways and mechanism of gating. *Nature* **584**, 646–651 (2020).
5. C. Ambrosi *et al.*, Pannexin1 and Pannexin2 channels show quaternary similarities to connexons and different oligomerization numbers from each other. *J. Biol. Chem.* **285**, 24420–24431 (2010).
6. S. Locovei, L. Bao, G. Dahl, Pannexin 1 in erythrocytes: Function without a gap. *Proc. Natl. Acad. Sci. U.S.A.* **103**, 7655–7659 (2006).
7. Y.-H. Chiu, K. S. Ravichandran, D. A. Bayliss, Intrinsic properties and regulation of Pannexin 1 channel. *Channels (Austin)* **8**, 103–109 (2014).
8. G. E. Sosinsky *et al.*, Pannexin channels are not gap junction hemichannels. *Channels (Austin)* **5**, 193–197 (2011).
9. G. Dahl, R. W. Keane, Pannexin: From discovery to bedside in 11±4 years? *Brain Res.* **1487**, 150–159 (2012).
10. S. Penuela *et al.*, Pannexin 1 and pannexin 3 are glycoproteins that exhibit many distinct characteristics from the connexin family of gap junction proteins. *J. Cell Sci.* **120**, 3772–3783 (2007).
11. F. Vanden Abeele *et al.*, Functional implications of calcium permeability of the channel formed by pannexin 1. *J. Cell Biol.* **174**, 535–546 (2006).
12. C. P. K. Lai *et al.*, Tumor-suppressive effects of pannexin 1 in C6 glioma cells. *Cancer Res.* **67**, 1545–1554 (2007).
13. M. Ishikawa *et al.*, Pannexin 3 functions as an ER Ca(2+) channel, hemichannel, and gap junction to promote osteoblast differentiation. *J. Cell Biol.* **193**, 1257–1274 (2011).
14. G. Sahu, S. Sukumaran, A. K. Bera, Pannexins form gap junctions with electrophysiological and pharmacological properties distinct from connexins. *Sci. Rep.* **4**, 4955 (2014).
15. D. Boassa, F. Qiu, G. Dahl, G. Sosinsky, Trafficking dynamics of glycosylated pannexin 1 proteins. *Cell Commun. Adhes.* **15**, 119–132 (2008).
16. R. J. Thompson *et al.*, Activation of pannexin-1 hemichannels augments aberrant bursting in the hippocampus. *Science* **322**, 1555–1559 (2008).
17. M.-C. Kienitz, K. Bender, R. Dermietzel, L. Pott, G. Zoidl, Pannexin 1 constitutes the large conductance cation channel of cardiac myocytes. *J. Biol. Chem.* **286**, 290–298 (2011).
18. W. Ma *et al.*, Pannexin 1 forms an anion-selective channel. *Pflugers Arch.* **463**, 585–592 (2012).
19. Y.-H. Chiu *et al.*, A quantized mechanism for activation of pannexin channels. *Nat. Commun.* **8**, 14324 (2017).
20. S. R. Bond, C. C. Naus, The pannexins: Past and present. *Front. Physiol.* **5**, 58 (2014).
21. S. Penuela, R. Bhalla, K. Nag, D. W. Laird, Glycosylation regulates pannexin intermixing and cellular localization. *Mol. Biol. Cell* **20**, 4313–4323 (2009).
22. Y.-J. Huang *et al.*, The role of pannexin 1 hemichannels in ATP release and cell-cell communication in mouse taste buds. *Proc. Natl. Acad. Sci. U.S.A.* **104**, 6436–6441 (2007).
23. R. A. Somerville, L. A. Ritchie, Differential glycosylation of the protein (PrP) forming scrapie-associated fibrils. *J. Gen. Virol.* **71**, 833–839 (1990).
24. A. K. Kumagai, K. J. Dwyer, W. M. Pardridge, Differential glycosylation of the GLUT1 glucose transporter in brain capillaries and choroid plexus. *Biochim. Biophys. Acta* **1193**, 24–30 (1994).
25. Y. van Kooyk, G. A. Rabinovich, Protein-glycan interactions in the control of innate and adaptive immune responses. *Nat. Immunol.* **9**, 593–601 (2008).
26. T. J. Hahn, C. F. Goochee, Growth-associated glycosylation of transferrin secreted by HepG2 cells. *J. Biol. Chem.* **267**, 23982–23987 (1992).
27. E. J. Choi, N. Palacios-Prado, J. C. Sáez, J. Lee, Identification of Cx45 as a major component of GJs in HeLa cells. *Biomolecules* **10**, 1389 (2020).
28. F. F. Bukauskas *et al.*, Clustering of connexin 43-enhanced green fluorescent protein gap junction channels and functional coupling in living cells. *Proc. Natl. Acad. Sci. U.S.A.* **97**, 2556–2561 (2000).
29. M. P. Silva, C. G. Rodrigues, W. A. Varanda, R. A. Nogueira, Memory in ion channel kinetics. *Acta Biotheor.* **69**, 697–722 (2021).
30. Y. Landesman *et al.*, Innexin-3 forms connexin-like intercellular channels. *J. Cell Sci.* **112**, 2391–2396 (1999).
31. A. Majewska, R. Yuste; M. A., Topology of gap junction networks in *C. elegans. J. Theor. Biol.* **212**, 155–167 (2001).
32. Q. Liu, B. Chen, E. Gaier, J. Joshi, Z. W. Wang, Low conductance gap junctions mediate specific electrical coupling in body-wall muscle cells of *Caenorhabditis elegans. J. Biol. Chem.* **281**, 7881–7889 (2006).
33. P. Liu *et al.*, Six innexins contribute to electrical coupling of *C. elegans* body-wall muscle. *PLoS One* **8**, e76877 (2013).
34. K. T. Simonsen, D. G. Moerman, C. C. Naus, Gap junctions in *C. elegans. Front. Physiol.* **5**, 40 (2014).
35. Q. Liu *et al.*, Gap junction networks in mushroom bodies participate in visual learning and memory in *Drosophila. eLife* **5**, 1–18 (2016).
36. T. A. Starich, J. Xu, I. M. Skerrett, B. J. Nicholson, J. E. Shaw, Interactions between innexins UNC-7 and UNC-9 mediate electrical synapse specificity in the Caenorhabditis elegans locomotory nervous system. *Neural Dev.* **4**, 16 (2009).
37. J. Wang, G. Dahl, Pannexin1: A multifunction and multiconductance and/or permeability membrane channel. *Am. J. Physiol. Cell Physiol.* **315**, C290–C299 (2018).
38. J. Wang, D. G. Jackson, G. Dahl, Cationic control of Panx1 channel function. *Am. J. Physiol. Cell Physiol.* **315**, C279–C289 (2018).
39. W. Ma, H. Hui, P. Pelegrin, A. Surprenant, Pharmacological characterization of pannexin-1 currents expressed in mammalian cells. *J. Pharmacol. Exp. Ther.* **328**, 409–418 (2009).
40. L. Bao, S. Locovei, G. Dahl, Pannexin membrane channels are mechanosensitive conduits for ATP. *FEBS Lett.* **572**, 65–68 (2004).
41. J. Wang *et al.*, The membrane protein Pannexin1 forms two open-channel conformations depending on the mode of activation. *Sci. Signal.* **7**, ra69 (2014).
42. S. F. Okada *et al.*, Coupled nucleotide and mucin hypersecretion from goblet-cell metaplastic human airway epithelium. *Am. J. Respir. Cell Mol. Biol.* **45**, 253–260 (2011).
43. C. A. Villalba-Galea, A. T. Chiem, Hysteretic behavior in voltage-gated channels. *Front. Pharmacol.* **11**, 579596 (2020).
44. M. Snipas, T. Kraujalis, N. Paulauskas, K. Maciunas, F. F. Bukauskas, Stochastic model of gap junctions exhibiting rectification and multiple closed states of slow gates. *Biophys. J.* **110**, 1322–1333 (2016).
45. X. López *et al.*, A physiologic rise in cytoplasmic calcium ion signal increases pannexin1 channel activity via a C-terminus phosphorylation by CaMKII. *Proc. Natl. Acad. Sci. U.S.A.* **118**, e2108967118 (2021).
46. G. D. Cymes, Y. Ni, C. Grosman, Probing ion-channel pores one proton at a time. *Nature* **438**, 975–980 (2005).
47. M. I. Niemeyer *et al.*, Neutralization of a single arginine residue gates open a two-pore domain, alkali-activated K+ channel. *Proc. Natl. Acad. Sci. U.S.A.* **104**, 666–671 (2007).
48. R. A. Romanov *et al.*, The ATP permeability of pannexin 1 channels in a heterologous system and in mammalian taste cells is dispensable. *J. Cell Sci.* **125**, 5514–5523 (2012).
49. G. Kanaporis, P. R. Brink, V. Valiunas, Gap junction permeability: Selectivity for anionic and cationic probes. *Am. J. Physiol. Cell Physiol.* **300**, C600–C609 (2011).
50. G. M. Carrow, I. B. Levitan, Selective formation and modulation of electrical synapses between cultured Aplysia neurons. *J. Neurosci.* **9**, 3657–3664 (1989).
51. R. Bodmer, V. Verselis, I. B. Levitan, D. C. Spray, Electrotonic synapses between Aplysia neurons in situ and in culture: Aspects of regulation and measurements of permeability. *J. Neurosci.* **8**, 1656–1670 (1988).
52. F. F. Bukauskas, A. B. Angele, V. K. Verselis, M. V. L. Bennett, Coupling asymmetry of heterotypic connexin 45/ connexin 43-EGFP gap junctions: Properties of fast and slow gating mechanisms. *Proc. Natl. Acad. Sci. U.S.A.* **99**, 7113–7118 (2002).
53. V. A. Skeberdis, L. Rimkute, A. Skeberdyte, N. Paulauskas, F. F. Bukauskas, pH-dependent modulation of connexin-based gap junctional uncouplers. *J. Physiol.* **589**, 3495–3506 (2011).
54. V. K. Verselis, M. V. Bennett, T. A. Bargiello, A voltage-dependent gap junction in *Drosophila melanogaster. Biophys. J.* **59**, 114–126 (1991).
55. D. Churchill, S. Caveney, Double whole-cell patch-clamp characterization of gap junctional channels in isolated insect epidermal cell pairs. *J. Membr. Biol.* **135**, 165–180 (1993).
56. F. Bukauskas, C. Kempf, R. Weingart, Electrical coupling between cells of the insect *Aedes albopictus. J. Physiol.* **448**, 321–337 (1992).
57. H. Sadamoto, H. Takahashi, S. Kobayashi, H. Kondoh, H. Tokumaru, Identification and classification of innexin gene transcripts in the central nervous system of the terrestrial slug *Limax valentianus. PLoS One* **16**, e0244902 (2021).
58. X. Shi, D. L. Jarvis, Protein N-glycosylation in the baculovirus-insect cell system. *Curr. Drug Targets* **8**, 1116–1125 (2007).
59. R. B. Parker, J. J. Kohler, Regulation of intracellular signaling by extracellular glycan remodeling. *ACS Chem. Biol.* **5**, 35–46 (2010).
60. L. Ebihara, *Xenopus* connexin38 forms hemi-gap-junctional channels in the nonjunctional plasma membrane of *Xenopus* oocytes. *Biophys. J.* **71**, 742–748 (1996).
61. A. Beckmann, A. Grissmer, E. Krause, T. Tschernig, C. Meier, Pannexin-1 channels show distinct morphology and no gap junction characteristics in mammalian cells. *Cell Tissue Res.* **363**, 751–763 (2016).
62. M. Kuzuya *et al.*, Structures of human pannexin-1 in nanodiscs reveal gating mediated by dynamic movement of the N terminus and phospholipids. *Sci. Signal.* **15**, eabg6941 (2022).
63. H.-B. Zhao, Y. Zhu, C. Liang, J. Chen, Pannexin 1 deficiency can induce hearing loss. *Biochem. Biophys. Res. Commun.* **463**, 143–147 (2015).
64. J. Chen, C. Liang, L. Zong, Y. Zhu, H.-B. Zhao, Knockout of pannexin-1 induces hearing loss. *Int. J. Mol. Sci.* **19**, 1332 (2018).
65. S. Petric *et al.*, Pannexin-1 deficient mice have an increased susceptibility for atrial fibrillation and show a QT-prolongation phenotype. *Cell. Physiol. Biochem.* **38**, 487–501 (2016).
66. K. Kranz *et al.*, Expression of Pannexin1 in the outer plexiform layer of the mouse retina and physiological impact of its knockout. *J. Comp. Neurol.* **521**, 1119–1135 (2013).
67. V. M. Kovalzon *et al.*, Sleep-wakefulness cycle and behavior in pannexin1 knockout mice. *Behav. Brain Res.* **318**, 24–27 (2017).
68. M. S. Aquilino *et al.*, Pannexin-1 deficiency decreases epileptic activity in mice. *Int. J. Mol. Sci.* **21**, 7510 (2020).
69. A. O. Ardiles *et al.*, Pannexin 1 regulates bidirectional hippocampal synaptic plasticity in adult mice. *Front. Cell. Neurosci.* **8**, 326 (2014).
70. T. A. Zolnik, B. W. Connors, Electrical synapses and the development of inhibitory circuits in the thalamus. *J. Physiol.* **594**, 2579–2592 (2016).
71. S.-C. Lee, S. L. Patrick, K. A. Richardson, B. W. Connors, Two functionally distinct networks of gap junction-coupled inhibitory neurons in the thalamic reticular nucleus. *J. Neurosci.* **34**, 13170–13182 (2014).

72. A. Ray, G. Zoidl, S. Weickert, P. Wahle, R. Dermietzel, Site-specific and developmental expression of pannexin1 in the mouse nervous system. *Eur. J. Neurosci.* **21**, 3277–3290 (2005).

73. J. Sevetson, J. S. Haas, Asymmetry and modulation of spike timing in electrically coupled neurons. *J. Neurophysiol.* **113**, 1743–1751 (2015).

74. M. A. Riquelme *et al.*, The ATP required for potentiation of skeletal muscle contraction is released via pannexin hemichannels. *Neuropharmacology* **75**, 594–603 (2013).

75. L. A. Corvalán *et al.*, Injury of skeletal muscle and specific cytokines induce the expression of gap junction channels in mouse dendritic cells. *J. Cell. Physiol.* **211**, 649–660 (2007).

76. N. Palacios-Prado *et al.*, pH-dependent modulation of voltage gating in connexin45 homotypic and connexin45/connexin43 heterotypic gap junctions. *Proc. Natl. Acad. Sci. U.S.A.* **107**, 9897–9902 (2010).

77. S. Zhang *et al.*, Structure of the full-length human Pannexin1 channel and insights into its role in pyroptosis. *Cell Discov.* **7**, 30 (2021).

78. C. Tian *et al.*, ff19SB: Amino-acid-specific protein backbone parameters trained against quantum mechanics energy surfaces in solution. *J. Chem. Theory Comput.* **16**, 528–552 (2020).

79. C. J. Dickson *et al.*, Lipid14: The amber lipid force field. *J. Chem. Theory Comput.* **10**, 865–879 (2014).

80. W. L. Jorgensen, J. Chandrasekhar, J. D. Madura, R. W. Impey, M. L. Klein, Comparison of simple potential functions for simulating liquid water. *J. Chem. Phys.* **79**, 926–935 (1983).

81. I. S. Joung, T. E. Cheatham III, Determination of alkali and halide monovalent ion parameters for use in explicitly solvated biomolecular simulations. *J. Phys. Chem. B* **112**, 9020–9041 (2008).

82. J. Wang, R. M. Wolf, J. W. Caldwell, P. A. Kollman, D. A. Case, Development and testing of a general amber force field. *J. Comput. Chem.* **25**, 1157–1174 (2004).

83. J. Wang, W. Wang, P. A. Kollman, D. A. Case, Automatic atom type and bond type perception in molecular mechanical calculations. *J. Mol. Graph. Model.* **25**, 247–260 (2006).

84. W. Humphrey, A. Dalke, K. Schulten, VMD: Visual molecular dynamics. *J. Mol. Graph.* **14**, 33–38, 27–28 (1996).

85. D. A. Case *et al.*, The Amber biomolecular simulation programs. *J. Comput. Chem.* **26**, 1668–1688 (2005).

86. T. Darden, D. York, L. Pedersen, Particle mesh Ewald: An N $\oplus$log(N) method for Ewald sums in large systems. *J. Chem. Phys.* **98**, 10089–10092 (1983).

87. G. Bussi, D. Donadio, M. Parrinello, Canonical sampling through velocity rescaling. *J. Chem. Phys.* **126**, 014101 (2007).

88. H. J. C. Berendsen, J. P. M. Postma, W. F. van Gunsteren, A. DiNola, J. R. Haak, Molecular dynamics with coupling to an external bath. *J. Chem. Phys.* **81**, 3684 (1984).

89. S. Izrailev, A. R. Crofts, E. A. Berry, K. Schulten, Steered molecular dynamics simulation of the Rieske subunit motion in the cytochrome bc(1) complex. *Biophys. J.* **77**, 1753–1768 (1999).

90. Schrödinger, Maestro (Schrödinger, LLC, New York, 2021).

91. J. Norberg, N. Foloppe, L. Nilsson, Intrinsic relative stabilities of the neutral tautomers of arginine side-chain models. *J. Chem. Theory Comput.* **1**, 986–993 (2005).

92. C. Møller, M. S. Plesset, Note on an approximation treatment for many-electron systems. *Phys. Rev.* **46**, 618 (1934).

93. A. D. Becke, Density-functional thermochemistry. III. The role of exact exchange. *J. Chem. Phys.* **98**, 5648 (1993).

94. J. B. Foresman, T. A. Keith, K. B. Wiberg, J. Snoonian, M. J. Frisch, Solvent effects. 5. Influence of cavity shape, truncation of electrostatics, and electron correlation on ab initio reaction field calculations. *J. Phys. Chem.* **100**, 16098–16104 (1996).

95. M. J. Frisch *et al.*, Gaussian 09 Revision A.02 (Gaussian, Inc., Wallingford, CT, 2016).